Design and experiment of dual micro-vibration isolation system for optical satellite flywheel

Shanbo Chen [a,b,c], Ming Xuan [a,b,c], Jian Xin [c], Yong Liu [c], Song Gu [a,b,c], Ji Li [a,b,c], Lei Zhang [a,b,c,*]

[a] Changchun Institute of Optics, Fine Mechanics and Physics, Chinese Academy of Sciences, Changchun 130033, China
[b] University of Chinese Academy of Sciences, Beijing 100049, China
[c] Chang Guang Satellite Technology LTD, Changchun 130033, China

ARTICLE INFO

ABSTRACT

This paper builds a dual isolation system for suppressing the micro-vibration due to flywheel of optical satellite. The advantages of this system compared to the single-layer vibration isolation system are: 1) the layout of flywheels is more compact, which improves the utilization rate of structure; 2) the load path of the perturbation of flywheel is extended; 3) the attenuation rate of vibration in high frequency band is improved. The transmissibility of force is discussed and the decay time of precession associated with the flywheel gyroscopic effect is analyzed. The suitable cut-off frequencies of isolators are designed in consideration of the precession decay time and the first-order natural frequency of the satellite during launch process. The influence of flywheel micro-vibration on camera with and without isolation is compared by on-ground optical imaging test. The RMS of pixel offset attenuates obviously under dual isolation and the maximum attenuation rate reaches 69.0%. The pixel offset value under dual isolation is less than 0.1 pixels, indicating the feasibility of dual isolation system for flywheel.

1. Introduction

Along with the rapid development of earth observational technology, satellites have very precise optical instruments used for various missions, putting forward higher requirements of the stability and pointing accuracy of optical satellites [1]. The flywheel is selected as the attitude control actuator, which is widely used in various space missions due to its high reliability and control accuracy [2]. However, owing to the unbalance of the rotor, the flywheel inevitably produces perturbation under working condition [3]. Micro-vibration will lead to line-of-sight jitter, resulting in blurred or distortion of images [4].

Micro-vibration suppression is always a key technology in the development of high-resolution optical satellites [5]. Considering the limited space and launch weight of micro satellite, it is more feasible to choose passive isolation as flywheel perturbation suppression scheme. Passive single-layer vibration isolation system for flywheel has been successfully used in some high-precision optical satellites. The Hubble telescope launched in 1990 adopts a passive isolation system employing metal springs in parallel with viscous fluid dampers to suppress the flywheel disturbance [6]. The cut-off frequency of the system is 18–20 Hz and the damping ratio is about 4%. FY-4 satellite launched in 2016 designs a Stewart platform-based passive isolation system. The attenuation rate of the system can be more than 70% for disturbance above 40 Hz [7]. The GOES-R satellite launched in 2016 designs a passive vibration

isolator based on viscoelastic material having an attenuation effect on flywheel disturbance above 50 Hz [8]. The theory of vibration isolation shows that the lower the natural frequency of isolator, the better the effect of vibration reduction. However, due to the high rotational speed of the rotor, the gyroscopic effect will cause a precession modal with low natural frequency [9]. As the modal is excited by the motion of the satellite, it becomes another low frequency disturbance source, which extends the stability time of attitude control [10–13]. The low frequency of isolator may influence the first-order natural frequency of the satellite during launch process, resulting in failing to withstand the launch vibration environment.

The perturbation of flywheel has the characteristics of small amplitude and wide frequency band, requiring high sensitivity of test equipment [14–16]. The measurement system based on Kistler Table is commonly used to test the flywheel perturbation. The system can directly measure the disturbing force and disturbing moment of the flywheel mounted on the platform [17]. However, the influence of micro-vibration on the image performance of the camera needs to be further evaluated. At present, the commonly on-ground test methods include optical imaging test and acceleration sensor-based jitter measurements [17,18]. Both methods simulate the condition of the camera in orbit to show the influence of micro-vibrations.

GF03 is a micro optical satellite designed with the principle of "low weight, low power consumption and high resolution" (as shown in

---

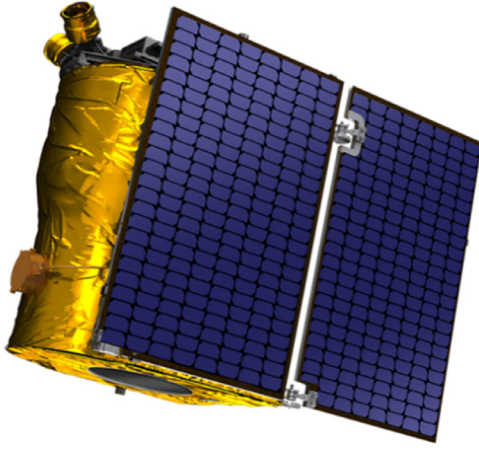Fig. 1. GF03 optical satellite model.

Fig. 2. Schematic diagram of the dual isolation system.

Fig. 1). The designed orbit of the satellite is 535 km sun-synchronous orbit, the resolution of sub-satellite point is better than 1 m and the launch weight of the whole satellite is less than 40 kg. This paper focuses on finding the proper cut-off frequency of isolators for flywheel with its impacts on attitude control taken into account [19]. Viscoelastic damping material is selected as an isolator. Its main parameters are designed by setting the appropriate temperature [20,21]. The pixel offset of camera with and without isolation is compared by the on-ground optical imaging test to quantitatively evaluate the vibration reduction

Substitute Eq. (2) into Eq. (1):

$$
\begin{cases}
\left(-m_1\omega^2 + c_1 i\omega + k_1\right)B_1 e^{i(\omega t-\varphi)} - \left(c_1 i\omega + k_1\right)B_2 e^{i(\omega t-\varphi)} = F_1 e^{i\omega t} \\
\left(-c_1 i\omega - k_1\right)B_1 e^{i(\omega t-\varphi)} + \left(-m_2\omega^2 + c_1 i\omega + k_1 + c_2 i\omega + k_2\right)B_2 e^{i(\omega t-\varphi)} = 0
\end{cases}
\tag{3}
$$

Solve the Eq. (3) and yield:

$$
B_2 = \frac{k_1 + c_1 i\omega}{\left(k_1 + k_2\right) - m_2\omega^2 + \left(c_1 + c_2\right)i\omega}B_1
\tag{4}
$$

$$
B_1 e^{-i\varphi} = \frac{\left(k_1 + k_2\right) - m_2\omega^2 + \left(c_1 + c_2\right)i\omega}{\left(k_1 - m_1\omega^2\right)\left(k_2 - m_2\omega^2\right) - \omega^2\left(m_1 k_1 + c_1 c_2\right) + i\omega\left(k_1 c_2 + k_2 c_1 - m_1\omega^2 c_1 - m_1\omega^2 c_2 - m_2\omega^2 c_1\right)}F_1
\tag{5}
$$

$$
B_2 e^{-i\varphi} = \frac{k_1 + c_1 i\omega}{\left(k_1 - m_1\omega^2\right)\left(k_2 - m_2\omega^2\right) - \omega^2\left(m_1 k_1 + c_1 c_2\right) + i\omega\left(k_1 c_2 + k_2 c_1 - m_1\omega^2 c_1 - m_1\omega^2 c_2 - m_2\omega^2 c_1\right)}F_1
\tag{6}
$$

efficiency. At last, the on-orbit rotational speed of flywheel is obtained through telemetry data and the pixel offset of the image is analyzed to verify the feasibility of dual isolation for flywheel [22,23].

2. Dual vibration isolation

In order to obtain higher vibration reduction efficiency, the dual vibration isolation theory is studied [24]. The evolution from the ideal single isolation system to the dual isolation system will inevitably insert the intermediate mass on the original ideal single isolation model, adding a resonance peak to the whole isolation system. The dual isolation system in single direction is shown in Fig. 2.

The dynamics of dual isolation system are described as:

$$
\begin{cases}
m_1\ddot{x}_1 + c_1\left(\dot{x}_1 - \dot{x}_2\right) + k_1\left(x_1 - x_2\right) = F_1 sin\omega t \\
m_2\ddot{x}_2 - c_1\left(\dot{x}_1 - \dot{x}_2\right) - k_1\left(x_1 - x_2\right) + c_2\dot{x}_2 + k_2 x_2 = 0
\end{cases}
\tag{1}
$$

As the isolated object is the source of vibration, the transmissibility μ is defined as the ratio of the initial excitation force and the force applied to the satellite.

$$
\mu = \frac{\left|F_f\right|}{\left|F_0\right|}
\tag{7}
$$

where F_0 represents the initial excitation force, F_f represents the force applied to the satellite:

$$
F_0 = F_1 sin\omega t
\tag{8}
$$

$$
F_f = c_2\dot{x}_2 + k_2 x_2
\tag{9}
$$

Then Eq. (7) can be solved as:

$$
\mu = \sqrt{\frac{\left(k_1 k_2 - \omega^2 c_1 c_2\right)^2 + \omega^2\left(k_1 c_2 + k_2 c_1\right)^2}{\left[\left(k_1 - m_1\omega^2\right)\left(k_2 - m_2\omega^2\right) - \omega^2\left(m_1 k_1 + c_1 c_2\right)\right]^2 + \omega^2\left(k_1 c_2 + k_2 c_1 - m_1\omega^2 c_1 - m_1\omega^2 c_2 - m_2\omega^2 c_1\right)^2}}
\tag{10}
$$

where m_1 and m_2 are the mass of flywheel and the intermediate layer, respectively; k_1 and c_1 are the stiffness and damping coefficient of the first isolator, respectively; k_2 and c_2 are the stiffness and damping coefficient of the second isolator, respectively; $F_1 sin\omega t$ represents the input perturbation from the flywheel.

Assume an exponential solution:

$$
\begin{cases}
x_1 = B_1 e^{i(\omega t-\varphi)} \\
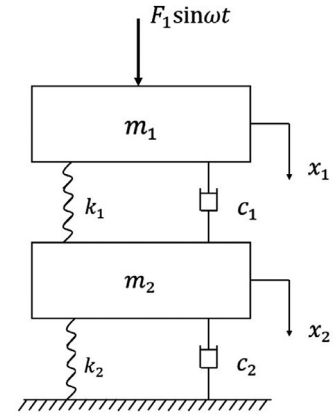x_2 = B_2 e^{i(\omega t-\varphi)}
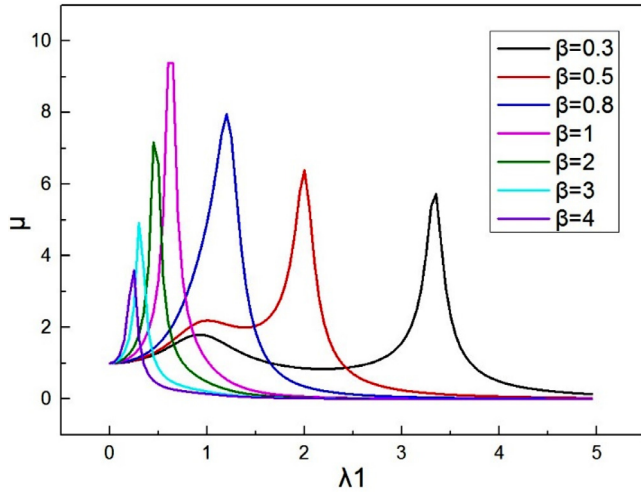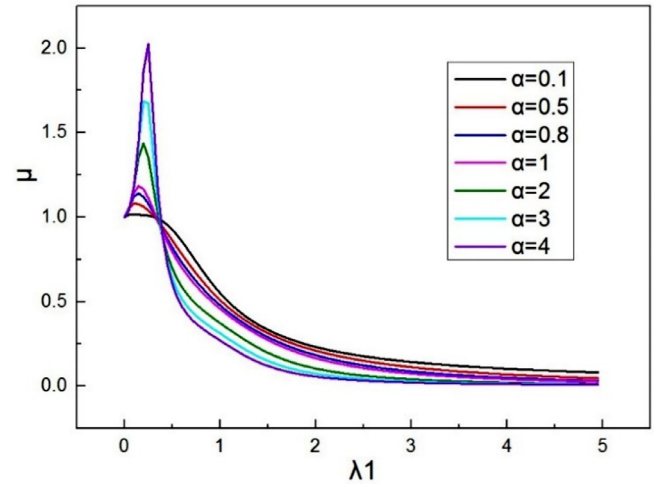\end{cases}
\tag{2}
$$

The mass ratio is defined as:

$$
\alpha = \frac{m_2}{m_1}
\tag{11}
$$

The modal frequency of each layer is defined as:

$$
\omega_1 = \sqrt{\frac{k_1}{m_1}}
\tag{12}
$$

$$
\omega_2 = \sqrt{\frac{k_2}{m_2}}
\tag{13}
$$

Fig. 3. The transmissibility of force under different β.

Fig. 4. The transmissibility of force under different α.

Define two dimensionless parameters:
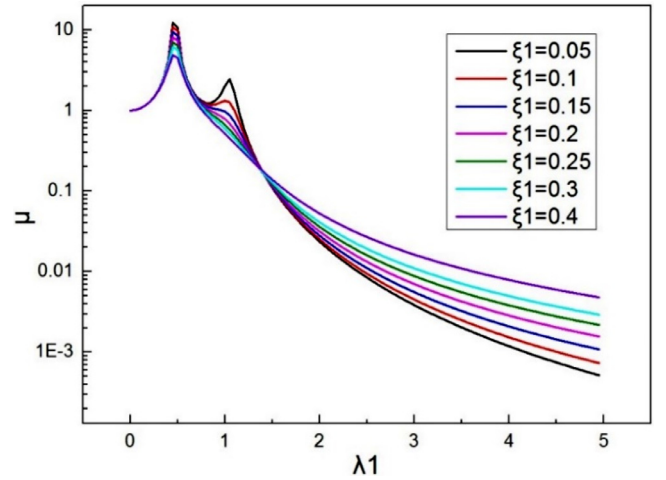
$$\lambda_1 = \frac{\omega}{\omega_1} \tag{14}$$

$$\lambda_2 = \frac{\omega}{\omega_2} \tag{15}$$

The damping ratio of each layer is defined as:

$$\xi_1 = \frac{c_1}{2\sqrt{m_1 k_1}} \tag{16}$$

$$\xi_2 = \frac{c_2}{2\sqrt{m_2 k_2}} \tag{17}$$

Substitute Eq. (11)–(17) into Eq. (10) and yield:

Fig. 5. The transmissibility of force under different ξ_1.

$$\mu = \sqrt{\frac{1 + 4\xi_1^2\lambda_1^2 + 4\xi_2^2\lambda_2^2 + 16\xi_1^2\xi_2^2\lambda_1^2\lambda_2^2}{\left[\left(1-\lambda_1^2\right)\left(1-\lambda_2^2\right) - \left(\frac{\lambda_2^2}{\alpha} + 4\xi_1\xi_2\lambda_1\lambda_2\right)\right]^2 + 4\left(\xi_1\lambda_1 + \xi_2\lambda_2 - \frac{\alpha+1}{\alpha}\xi_1\lambda_1\lambda_2^2 - \xi_2\lambda_1^2\lambda_2\right)^2}} \tag{18}$$

Define a dimensionless parameter:

$$\beta = \frac{\lambda_2}{\lambda_1} = \frac{\omega_1}{\omega_2} \tag{19}$$

Substitute Eq. (19) into Eq. (18) and the final expression of μ is attained as follows:

Fig. 4 shows the transmissibility μ with respect to λ_1 under different α, in which $\beta = 3.5$, $\xi_1 = 0.4$, and c_2 equals to c_1. The attenuation rate becomes faster with the increasing α, but the amplitude of the resonance peak gradually becomes larger. Therefore, the value of α should be designed in consideration of the attenuation rate and the formant amplitude.

$$\mu = \sqrt{\frac{1 + 4\xi_1^2\lambda_1^2 + 4\xi_2^2\beta^2\lambda_1^2 + 16\xi_1^2\xi_2^2\beta^2\lambda_1^4}{\left[\left(1-\lambda_1^2\right)\left(1-\beta^2\lambda_1^2\right) - \left(\frac{\beta^2\lambda_1^2}{\alpha} + 4\xi_1\xi_2\beta\lambda_1^2\right)\right]^2 + 4\left(\xi_1\lambda_1 + \xi_2\beta\lambda_1 - \frac{\alpha+1}{\alpha}\xi_1\lambda_1\beta^2\lambda_1^2 - \xi_2\lambda_1^2\beta\lambda_1\right)^2}} \tag{20}$$

Fig. 3 shows the transmissibility μ with respect to λ_1 under different β, in which $\alpha = 11$, $\xi_1 = 0.4$, and c_2 equals to c_1. The frequency of the resonance peak gradually decreases with an increased β. When $\beta < 1$, the amplitude of the resonance peak becomes larger with an increased β, while $\beta > 1$, the amplitude of the resonance peak becomes smaller with an increased β. Moreover, the larger the value of β, the smaller the frequency range of the amplification region and the faster the peak attenuation rate. Therefore, β should be increased as much as possible to obtain a higher reduction efficiency.

Fig. 5 shows the transmissibility μ with respect to λ_1 under different ξ_1, in which $\alpha = 11$, $\beta = 2$ and c_2 equals to c_1. Here, the damping coefficient of the two layers isolators are the same and the larger the ξ_1, the better the formant attenuation effect. However, the attenuation rate lowers with the increasing ξ_1, indicating that the value of ξ_1 should be designed in consideration of the attenuation rate and the formant amplitude.

From Figs. 4 and 5, both α and ξ_1 should be designed in consideration of the vibration attenuation rate and the formant amplitude. However,
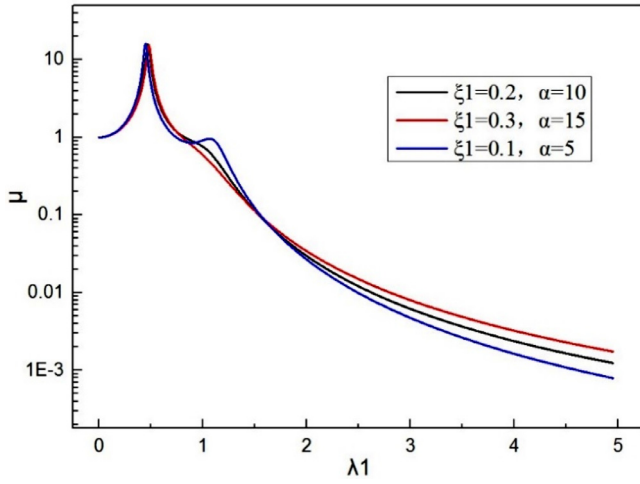
Fig. 6. The transmissibility of force under different α and ξ_1.

α and ξ_1 have opposite effects on the attenuation rate and the formant amplitude. To obtain optimized parameters of the dual vibration isolation system, it is necessary to compare the influence efficiency of α and ξ_1 [25]. The transmissibility μ with respect to λ_1 is calculated with $\beta = 2$, $\alpha = 10$ and $\xi_1 = 0.2$, then the transmissibility of increasing and decreasing the value of α with ξ_1 at the same time by 50% are calculated and compared under the condition of unchanged β. The comparisons are shown in Fig. 6. It shows that the resonance peak decreases 2.42% and the attenuation rate at $\lambda_1 = 4.95$ decreases 0.05% with increased α and ξ_1, the resonance peak increases 2.86% and the attenuation rate at $\lambda_1 = 4.95$ increases 0.04% with decreased α and ξ_1. Combining with the single effects of α or ξ_1 on the attenuation rate and the formant amplitude, it can be concluded that under the condition of unchanged β, the higher vibration attenuation rate can be obtained by preferentially reducing the value of ξ_1, and the lower formant amplitude can be obtained by preferentially reducing the value of α.

3. Precession of flywheel

The flywheel is mainly composed of rotor and shell, which is shown as Fig. 7.

The dynamic of flywheel at steady rotational speed is described by the equation [26]:

$$M\ddot{x} + (C + G)\dot{x} + Kx = F \tag{21}$$

In Eq. (21), **M**, **K**, **C**, **G** are 6×6 system matrixes of mass, stiffness, damping and gyroscope, x is the displacement vector and F is the perturbation vector, which can be expressed as follows:

$$\mathbf{M} = \mathrm{diag}\begin{bmatrix} m & m & m & I^x & I^y & I^z_{shell} \end{bmatrix} \tag{22}$$
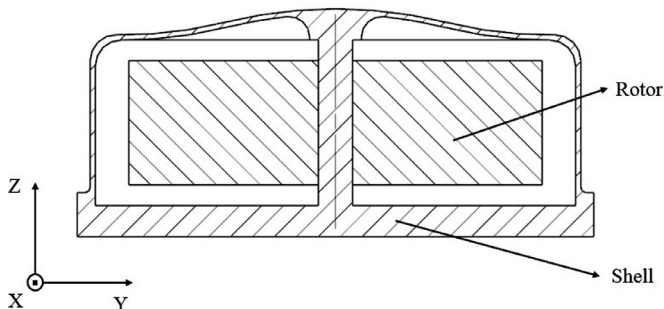
Fig. 7. Section view and the coordinate system definition of the flywheel.

$$\mathbf{K} = \mathrm{diag}\begin{bmatrix} k_{11} & k_{22} & k_{33} & k_{44} & k_{55} & k_{66} \end{bmatrix} \tag{23}$$

$$\mathbf{C} = \mathrm{diag}\begin{bmatrix} c_{11} & c_{22} & c_{33} & c_{44} & c_{55} & c_{66} \end{bmatrix} \tag{24}$$

$$\mathbf{G} = \begin{bmatrix} 0 & 0 & 0 & 0 & 0 & 0 \\ 0 & 0 & 0 & 0 & 0 & 0 \\ 0 & 0 & 0 & 0 & 0 & 0 \\ 0 & 0 & 0 & 0 & 0 & 0 \\ 0 & 0 & 0 & 0 & 0 & I^z_{rotor} \\ 0 & 0 & 0 & 0 & -I^z_{rotor} & 0 \end{bmatrix} \tag{25}$$

$$x = \begin{bmatrix} u^x & u^y & u^z & \theta^x & \theta^y & \theta^z \end{bmatrix}^T \tag{26}$$

where m represents the mass of flywheel; I represents the inertia of flywheel, k_{ii} and c_{jj} represent the stiffness and damping coefficient of the isolation system, respectively; I_{rotor} and I_{shell} represent the inertia of the rotor and shell, respectively.

$$I = I_{rotor} + I_{shell} \tag{27}$$

Extract the radial rotational freedom and omit the perturbation vector, the Eq. (21) can be reduced to:

$$\begin{bmatrix} I^x & \\ & I^y \end{bmatrix}\begin{bmatrix} \ddot{\theta}_x \\ \ddot{\theta}_y \end{bmatrix} + \left\{ \begin{bmatrix} c_{44} & \\ & c_{55} \end{bmatrix} + \Omega\begin{bmatrix} & I^z_{rotor} \\ -I^z_{rotor} & \end{bmatrix} \right\}\begin{bmatrix} \dot{\theta}_x \\ \dot{\theta}_y \end{bmatrix} + \begin{bmatrix} k_{44} & \\ & k_{55} \end{bmatrix}\begin{bmatrix} \theta_x \\ \theta_y \end{bmatrix} = \begin{bmatrix} 0 \\ 0 \end{bmatrix} \tag{28}$$

For the symmetry configuration of the flywheel:

$$I^x = I^y \tag{29}$$

$$k_{44} = k_{55} \tag{30}$$

$$c_{44} = c_{55} \tag{31}$$

The modal frequency of the isolation system is defined as:

$$\omega_n = \sqrt{\frac{k_{44}}{I^x}} \tag{32}$$

The damping ratio of the isolation system is defined as:

$$\xi = \frac{c_{44}}{2\sqrt{I^x k_{44}}} \tag{33}$$

Substitute Eq. (32)-(33) into Eq. (28) and yield:

$$\begin{bmatrix} \ddot{\theta}_x \\ \ddot{\theta}_y \end{bmatrix} + \left\{ 2\xi\omega_n\begin{bmatrix} 1 & \\ & 1 \end{bmatrix} + \eta\Omega\begin{bmatrix} & 1 \\ -1 & \end{bmatrix} \right\}\begin{bmatrix} \dot{\theta}_x \\ \dot{\theta}_y \end{bmatrix} + \omega_n^2\begin{bmatrix} 1 & \\ & 1 \end{bmatrix}\begin{bmatrix} \theta_x \\ \theta_y \end{bmatrix} = \begin{bmatrix} 0 \\ 0 \end{bmatrix} \tag{34}$$

where,

$$\eta = \frac{I^z_{rotor}}{I^x} \tag{35}$$

The precession of flywheel mainly attributes to the momentum torque vector of rotor changed by the elastic restoring torque of isolation system. The second derivative term of the radial rotation angle of the flywheel in Eq. (34) can be omitted [27]. Then the approximate precession equation of the flywheel is obtained as:

$$\left\{ 2\xi\omega_n\begin{bmatrix} 1 & \\ & 1 \end{bmatrix} + \eta\Omega\begin{bmatrix} & 1 \\ -1 & \end{bmatrix} \right\}\begin{bmatrix} \dot{\theta}_x \\ \dot{\theta}_y \end{bmatrix} + \omega_n^2\begin{bmatrix} 1 & \\ & 1 \end{bmatrix}\begin{bmatrix} \theta_x \\ \theta_y \end{bmatrix} = \begin{bmatrix} 0 \\ 0 \end{bmatrix} \tag{36}$$

The characteristic polynomial of Eq. (36) is:

$$\rho(s) = \left(4\xi^2\omega_n^2 + \eta^2\Omega^2\right)\left(s^2 + \frac{4\xi\omega_n^3 s}{4\xi^2\omega_n^2 + \eta^2\Omega^2} + \frac{\omega_n^4}{4\xi^2\omega_n^2 + \eta^2\Omega^2}\right) \tag{37}$$

The modal frequency of precession is defined as:

$$\omega_p = \frac{\omega_n^2}{\sqrt{4\xi^2\omega_n^2 + \eta^2\Omega^2}} \tag{38}$$

The damping ratio of precession is defined as:

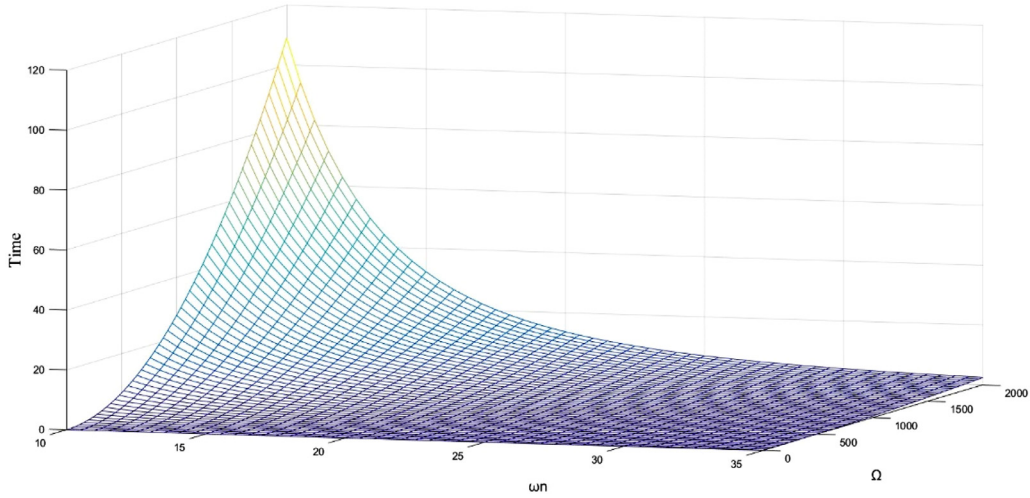$$\xi_p = \frac{2\xi\omega_n}{\sqrt{4\xi^2\omega_n^2 + \eta^2\Omega^2}} \tag{39}$$

Fig. 8. The decay time of precession under different parameter.

Fig. 8 shows that the decay time increases with the increasing Ω and decreases with the increasing ω_n.

4. Design of isolation system

4.1. Assembly of isolator

For the GF03 satellite, the flywheel is assembled on the electronic box through viscoelastic damping isolators rather than directly on the main structure of the satellite, and the electronic box is assembled on the main structure through the isolators with the same material. The advantage of this installation is that the load path of the perturbation of flywheel can be extended. Meanwhile, the electronic box acts as an intermediate mass and forms a dual vibration isolation system. The flywheel is shown in Fig. 9, the installation flange of flywheel is integrally designed with isolator. The installation of the flywheel isolator is shown in Fig. 10, where the isolator of the electronic box is installed with the same viscoelastic damping material selected.

4.2. Viscoelastic damping material

The viscoelastic damping material selected in this paper is silicone rubber (ZN-45), which has the advantages of large damping, low density and high stability. The result of dynamic thermomechanical analysis (DMA) of silicone rubber tested under 125 Hz is shown in Fig. 11. It can be seen from the figure that the modulus E and loss factor tan(δ) of silicone rubber vary greatly with temperature. The lower the temperature,

Fig. 9. Flywheel integrally designed with isolator.

Then the decay time of precession can be approximately calculated as:

$$T_p = \frac{4}{\xi_p \omega_p} = \frac{2\left(\xi^2 \omega_n^2 + \eta^2 \Omega^2\right)}{\xi \omega_n^3} \tag{40}$$

The waterfall plot of the decay time of precession with respect to ω_n and Ω is shown in Fig. 8, in which η is set as 1.4 and ξ is set as 0.04.
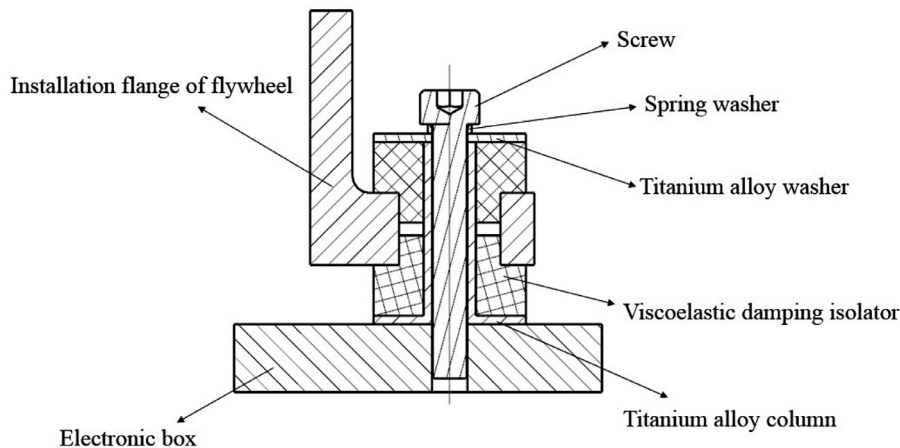
Fig. 10. Section view of the isolator assembly.
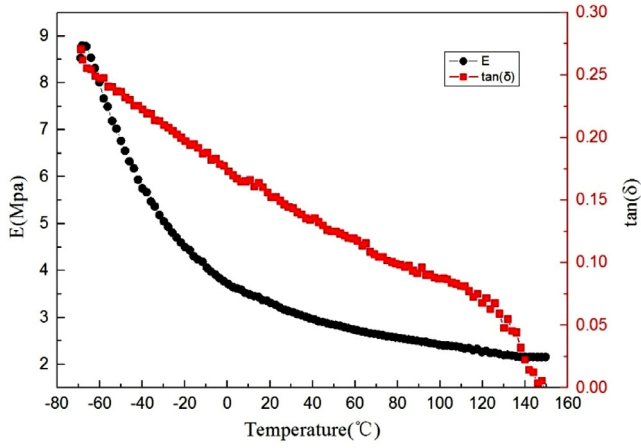
Fig. 11. The modulus and loss factor of silicone rubber varied with temperature.

Fig. 12. Limit of pixel offset for high-resolution camera.

Fig. 13. Comparison of transmissibility under single isolation and dual isolation.

the larger the modulus and damping of the material. Since the isolator is located in the cabin of the satellite, the ambient temperature is generally controlled between −20 ℃ and +40 ℃. Considering the cut-off frequency and damping ratio of the isolator and the feasibility of the thermal control scheme, the operating temperature of the material is chosen as 20 °C. Therefore, the isolator is controlled in the temperature range (20 ± 0.5 °C) by reasonable thermal control measures to make its performance meet the demand and not subject to the external environment temperature change.

4.3. Parameter design of isolation system

In order to meet the requirement of real-time attitude adjustment for satellite, the rotational speed of the flywheel needs to be constantly changed during working condition. Since the characteristics of flywheel disturbance are closely related to the rotational speed, the frequency and amplitude of the disturbance will change at different operating speeds. So, it is important to consider the uncertainties inherent to the external loading as well as the structural parameters in dealing with structural vibration control problem. In the low frequency band, the perturbation of the flywheel is dominated by the fundamental harmonic disturbance. The amplitude of the fundamental harmonic increases with the increasing rotational speed of flywheel. Therefore, the first-order natural frequency of the dual vibration isolation system should be reduced as long as the frequency requirement of the launch process is satisfied, so as to input a relatively small perturbation at the system resonance frequency. Vibration isolators developed for on-orbit observational application need to isolate micro-vibration when in orbit, and also withstand severe launch vibration environment [23]. The mass of flywheel is 0.9 kg and the mass of intermediate layer is 9 kg. It means that the mass of the dual isolation system has reached 10 kg, accounting for more than 25% of the total satellite weight. Therefore, the cut-off frequency of the dual isolation system will have a great impact on the first-order natural frequency of the satellite. Here, ω_1 is designed as 659.4 Hz and ω_2 is designed as 188.4 Hz. The first-order natural frequency of the satellite is calculated by the finite element simulation (Patran & Nastran) as 26.4 Hz, which satisfies the requirement of the CZ-11 rocket that the first-order natural frequency of the satellite higher than 25 Hz.

The pixel size of focal plane is 4.5 μm and the limits of pixel offset as optical design indicator for high-resolution camera in this article is shown in Fig. 12, showing that the limit of pixel offset is frequency dependent. The higher the frequency, the lower the amplitude of the pixel offset limited.

The comparison between the transmissibility of $\beta = 3.5$ (dual isolation) and $\beta = 0$ (single isolation) is shown in Fig. 13(Eq. (20)), where ξ_1 is set as 0.1. Fig. 13 shows the reduction efficiency of dual isolation
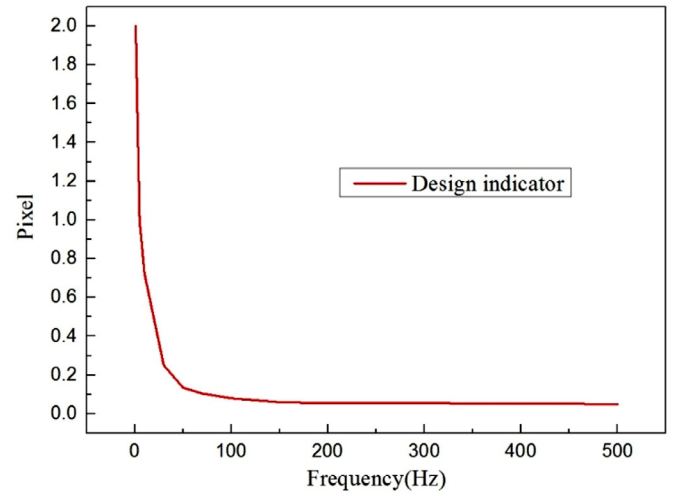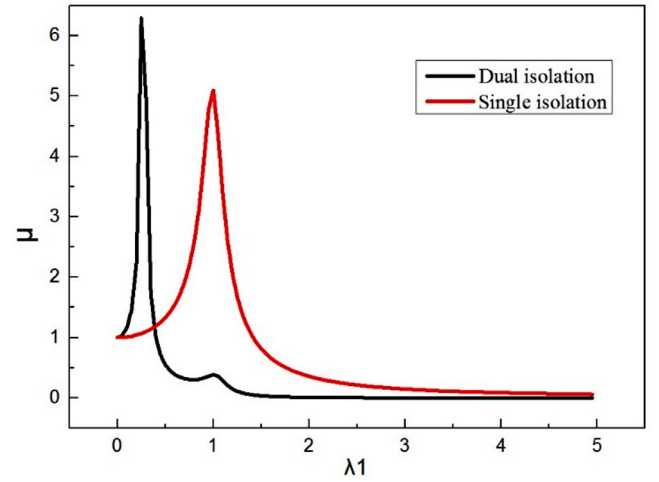
is much higher than single isolation. The vibration reduction effect can be generated when λ_1 is more than 1.4 for single isolation while 0.4 for dual isolation. Although the resonance peak of dual isolation is higher than single isolation, it can still meet the requirement by reasonable design.

The natural frequency of the first layer is much higher than the second layer of the dual isolation system. The isolator of the flywheel with the electronic box can be considered as part of the "shell" of flywheel. The first-order torsional natural frequency and damping ratio of the dual isolation system are analyzed as 43 Hz and 0.04 by simulation. The lateral inertia of system I_{system}^x is 0.05 kgm^2, then ω_n, ξ and η can be calculated by Eq. (32)–(35) respectively. The maximum rotational speed of the flywheel is 2000 rpm, the maximum decay time of precession can be derived as 0.003 s from Eq. (40), which is far less than the requirement of satellite maneuver stability time 60 s.

5. Experiment

5.1. Experimental apparatus

In this paper, the effect of micro-vibration on image motion is obtained by imaging test. The test platform is built to simulate the on-orbit imaging conditions. The satellite is suspended to a horizontal state using a low-frequency suspension system for the purpose of offsetting the ef-
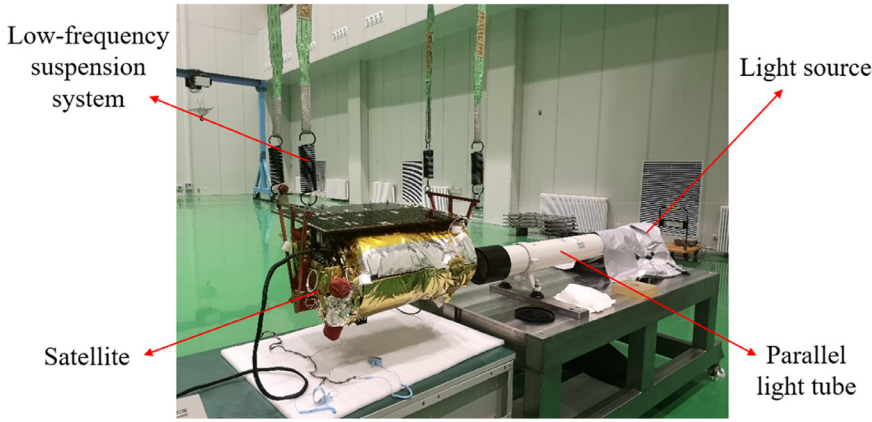
Fig. 14. On-ground imaging test platform.

(a) @100rpm

(b) @1000rpm

(c) @1500rpm

(d) @2000rpm

Fig. 15. Image of narrow line target.

fect of gravity on the test results. The on-ground test platform is shown in Fig. 14. Given that the first natural frequency of the satellite on orbit is 13 Hz (the solar array), the suspension system is tuned to give a 1 Hz axial isolation frequency, which is an order of magnitude softer. The narrow line target is illuminated by the light source through the paral-lel light tube to simulate the infinite distant object [18]. In the vicinity of the zero value of the flywheel angular velocity, its perturbations are most evident on the image quality, indicating a sharp change in the torque of dry friction forces effects. Therefore, it is necessary to ensure the flywheel working on-orbit in a stable speed range and the speed is limited to no passing through 0 rpm. The on-ground image is taken by the camera when the single working flywheel is under steady rotational speed from 100 rpm to 2000 rpm. The steady 0 rpm is tested to char-acterize the impact of environmental background noise disturbance on image quality. The images of narrow line target under dual isolation in some typical rotational speeds are shown in Fig. 15.

5.2. Data processing and results

Data processing for the imaging test is undertaken in a MATLAB en-vironment [17]. To analyze the vibration characteristics from the image, a grayscale threshold set at 90% of the maximum digital number is used to remove random noise. After removing the strip noise by a smoothing filter, the narrow line is then extracted from the image. The centroid of each row is calculated using arithmetic method [28]. The pixel off-set in the time domain could be obtained. Thus, the pixel offset in the frequency domain could be calculated by Fast Fourier Transform (FFT). For the single working Z-direction flywheel, the pixel offset of camera
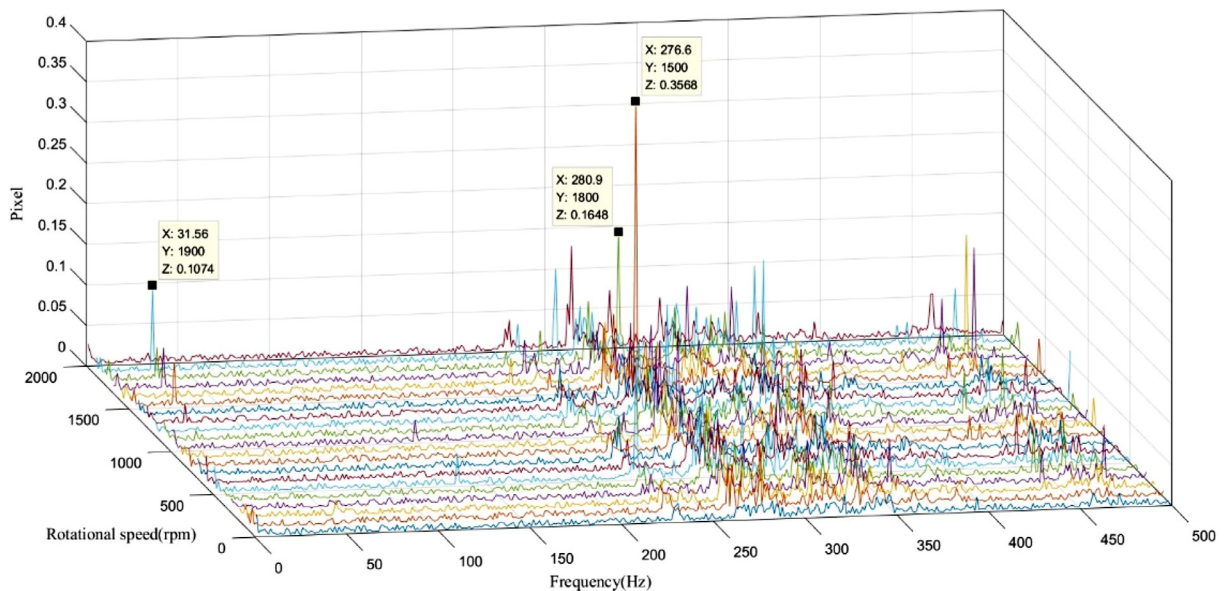

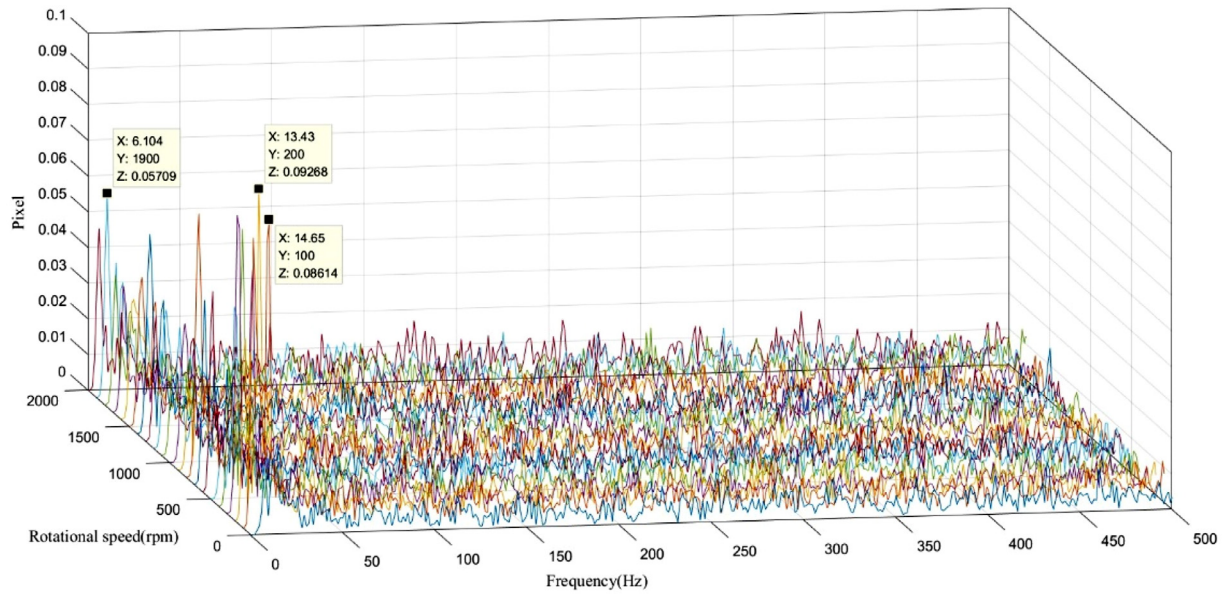**Fig. 16.** Pixel offset without isolation in the frequency domain.

Fig. 17. Pixel offset under dual isolation in the frequency domain.

(a) @100rpm

(b) @1000rpm
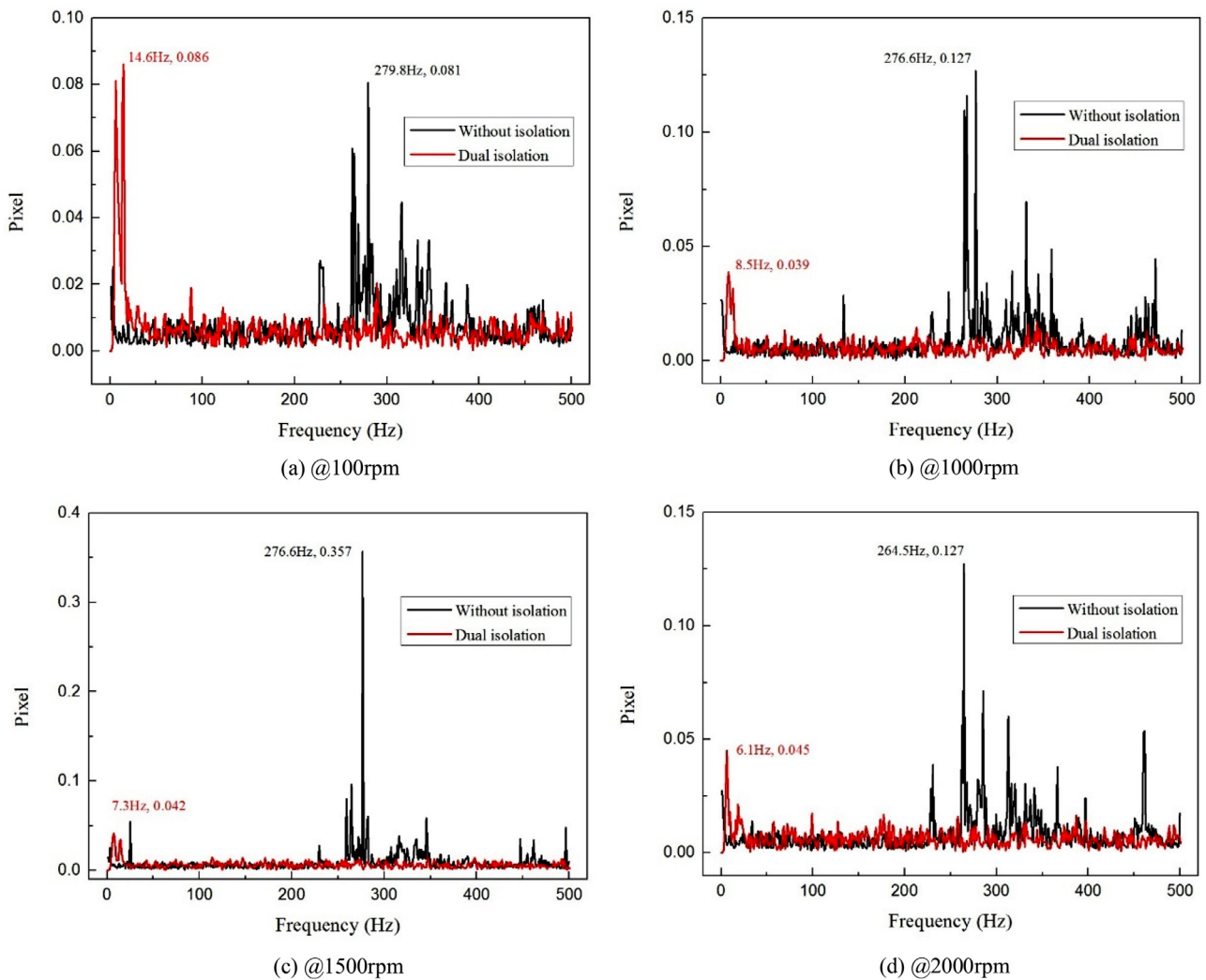
(c) @1500rpm

(d) @2000rpm

Fig. 18. Comparison of pixel offset with and without isolation.

Table 1
Pixel offset RMS data with and without isolation.

Flywheel rotational speed (rpm)	Without isolation (Pixel)	Dual isolation (Pixel)	Decay rate
100	0.0135	0.0109	19.3%
200	0.0153	0.0101	34.0%
300	0.0151	0.0096	36.4%
400	0.0158	0.0086	45.6%
500	0.0197	0.0084	57.4%
600	0.0150	0.0084	44.0%
700	0.0160	0.0067	58.1%
800	0.0140	0.0082	41.4%
900	0.0157	0.0073	53.5%
1000	0.0175	0.0073	58.3%
1100	0.0151	0.0067	55.6%
1200	0.0214	0.0074	65.4%
1300	0.0178	0.0068	61.8%
1400	0.0135	0.0081	40.0%
1500	0.0252	0.0078	69.0%
1600	0.0168	0.0070	58.3%
1700	0.0186	0.0067	64.0%
1800	0.0175	0.0079	54.9%
1900	0.0191	0.0085	55.5%
2000	0.0154	0.0077	50.0%

without isolation at different rotational speeds is shown in Fig. 16. As a comparison, the pixel offset under dual isolation is shown in Fig. 17. The pixel offset of some typical rotational speeds is compared in Fig. 18.

As shown in Fig. 16, the influence of micro-vibration of flywheel on this satellite is mainly focused on 200–400 Hz and 450–500 Hz without isolation. The flywheel micro-vibration has a great impact on the imaging of the high-resolution camera. The maximum resonance peak reaches 0.357 pixels in 276.6 Hz at 1500 rpm, which is far beyond the design indicator. It can be seen from Figs. 17 and 18 that the pixel offset attenuates obviously in high frequency band under dual isolation. In the low frequency band from 6 Hz to 15 Hz, the pixel offset is amplified, and the maximum resonance peak reaches 0.093 pixels in 13.4 Hz at 200 rpm, which is far less than the design indicator of 0.7 pixels from Fig. 12.

To further illustrate the reduction effect, the pixel offset root mean square (RMS) of each rotational speed with and without isolation along with the decay rate are listed in Table 1. The decay rate can be calculated as:

$$\Delta = \frac{P_w - P_d}{P_d} \qquad (41)$$

where P_w represents the pixel offset RMS value without isolation and P_d represents the pixel offset RMS value under dual isolation. The attenuation rate is above 19%, minimum is 19.3% at 100 rpm and maximum up to 69.0% at 1500 rpm.

6. Conclusions

(1) The reduction effect of dual vibration isolation is affected by many factors. The increasing β can reduce the resonance peak of transmissibility and the frequency range of the amplification region. The design of α and ξ_1 depends on the requirements of the attenuation rate or the amplitude of the resonance peak.

(2) The decay time of precession decreases with the increased natural frequency of isolation system and increases with the increased rotational speed of rotor.

(3) The modulus and damping of silicone rubber vary greatly with temperature. By adopting reasonable temperature control, the appropriate material properties can be selected to meet the requirements of the isolation system.

(4) The pixel offset of camera with and without isolation is compared by the on-ground optical imaging test, and the maximum attenuation rate of pixel offset RMS reaches 69.0% at 1500 rpm.

(5) The pixel offset value under dual isolation is less than 0.1 pixels, indicating the feasibility of dual micro-vibration isolation system for flywheel.

Declaration of Competing Interest

The authors declare that they have no known competing financial interests or personal relationships that could have appeared to influence the work reported in this paper.

CRediT authorship contribution statement

Shanbo Chen: Methodology, Writing - original draft. **Ming Xuan:** Supervision. **Jian Xin:** Software, Visualization. **Yong Liu:** Investigation, Data curation. **Song Gu:** Resources, Writing - review & editing. **Ji Li:** Software, Validation. **Lei Zhang:** Conceptualization, Writing - review & editing.

Acknowledgments

References

[1] Kim DK. Micro-vibration model and parameter estimation method of a reaction wheel assembly. J Sound Vib 2014;333:4214–31. doi:10.1016/j.jsv.2014.04.032.
[2] Lee DO, Yoon JS, Han JH. Development of integrated simulation tool for jitter analysis. Int J Aeronaut Sp Sci 2012;13:64–73. doi:10.5139/IJASS.2012.13.1.64.
[3] Hyde TT, Ha KQ, Johnston JD, Howard JM, Mosier GE. Integrated modeling activities for the James Webb space telescope: optical jitter analysis. Proc. SPIE 2004;5487:588. doi:10.1117/12.551806.
[4] Le TD, Ahn KK. Experimental investigation of a vibration isolation system using negative stiffness structure. Int J Mech Sci 2013;70:99–112. doi:10.1016/j.ijmecsci.2013.02.009.
[5] Yang J, Xu Z, Wu Q, Wang Z, Li H, He S. Design of a vibration isolation system for the space telescope. J Guid Control Dyn 2015;38:2441–8. doi:10.2514/1.G001221.
[6] Davis LP, Wilson JF, Jewell RE, Roden JJ. Hubble space telescope reaction wheel assembly vibration isolation system. Huntsville, Alabama: NASA Marshall Space Flight Center; 1986. p. 9.
[7] Freesland D, Carter D, Chapel J, Clapp B, Howat J, Krimchansky A. GOES-R dual isolation. 38th Annual AAS Guidance & Control Conference; 2015.
[8] Yao-Hai D, Xu-Bin Z, Jun-Feng S, Xing-Tian L, Yu Z-F. Study on micro-vibration suppression technology of fy-4 satellite. Aerosp. Shanghai 2017;34(4):20–7. doi:10.19328/j.cnki.1006-1630.2017.04.003.
[9] Addari D, Aglietti GS, Remedia M. Dynamic mass of a reaction wheel including gyroscopic effects: an experimental approach. AIAA J 2017;55:274–85. doi:10.2514/1.J055398.

[10] Vaillon L., Champetier C., Guillaud V., Alldridge J., Philippe C. Passive and active microvibration control for very high pointing accuracy space systems. Eur sp agency, Special Publ ESA SP 1997:497–503. doi:10.1088/0964-1726/8/6/302.

[11] Kajiwara I, Kitabatake S, Hosoya N, Maeda S. Design of dielectric elastomer actuators for vibration control at high frequencies. Int J Mech Sci 2019;157–158:849–57. doi:10.1016/j.ijmecsci.2019.05.019.

[12] Zhang Y, Sheng C, Hu Q, Li M, Guo Z, Qi R. Dynamic analysis and control application of vibration isolation system with magnetic suspension on satellites. Aerosp Sci Technol 2018;75:99–114. doi:10.1016/j.ast.2017.12.041.

[13] Marsh HC, Karpenko M, Gong Q. Relationships between maneuver time and energy for reaction wheel attitude control. J Guid Control Dyn 2018;41:335–48. doi:10.2514/1.G002843.

[14] Chen S, Chen Y, Zhang Z, Liu Y, Leng J. Experiment and analysis of morphing skin embedded with shape memory polymer composite tube. J Intell Mater Syst Struct 2014;25. doi:10.1177/1045389X13517307.

[15] Oh HU, Taniwaki S, Kinjyo N, Izawa K. Flywheel vibration isolation test using a variable-damping isolator. Smart Mater Struct 2006;15:365–70. doi:10.1088/0964-1726/15/2/017.

[16] Wang CG, Liu YP, Tan HF. Global and local interactive buckling behavior of a stiff film/compliant substrate system. Int J Solids Struct 2016. doi:10.1016/j.ijsolstr.2016.10.006.

[17] Chen SB, Xuan M, Zhang L, Gu S, Gong XX, Sun HY. Simulating and testing microvibrations on an optical satellite using acceleration sensor-based jitter measurements. Sensors 2019;19:1–13. doi:10.3390/s19081797.

[18] Li L, Tan L, Kong L, Wang D, Yang H. The influence of flywheel micro vibration on space camera and vibration suppression. Mech Syst Signal Process 2018;100:360–70. doi:10.1016/j.ymssp.2017.07.029.

[19] Guo J, Geng Y, Wu B, Kong X. Vibration suppression of flexible spacecraft during attitude maneuver using CMGs. Aerosp Sci Technol 2018;72:183–92. doi:10.1016/j.ast.2017.11.005.

[20] Bronowicki AJ. Vibration isolator for large space telescopes. J Spacecr Rockets 2006;43:45–53. doi:10.2514/1.12036.

[21] Liu Y, Guo K, Wang C, Gao H. Wrinkling and ratcheting of a thin film on cyclically deforming plastic substrate: mechanical instability of the solid-electrolyte interphase in Li–ion batteries. J Mech Phys Solids 2019. doi:10.1016/j.jmps.2018.08.006.

[22] Clapp B.R., Weigl H.J., Goodzeit N.E., Carter D.R., Rood T.J. GOES-R active vibration damping controller design, implementation, and on-orbit performance. CEAS Sp J 2018:1–17. doi:10.1007/s12567-017-0190-4.

[23] Lee DO, Park G, Han JH. Experimental study on on-orbit and launch environment vibration isolation performance of a vibration isolator using bellows and viscous fluid. Aerosp Sci Technol 2015;45:1–9. doi:10.1016/j.ast.2015.04.012.

[24] Yuhua S. Research on two-stage vibration isolation design method of powerpack in diesel railcar; 2013. p. 19–20.

[25] Yan WJ, Zhao MY, Sun Q, Ren WX. Transmissibility-based system identification for structural health monitoring: fundamentals, approaches, and applications. Mech Syst Signal Process 2019;117:453–82. doi:10.1016/j.ymssp.2018.06.053.

[26] Zhang Z, Aglietti GS, Ren W. Coupled microvibration analysis of a reaction wheel assembly including gyroscopic effects in its acceleration. J Sound Vib 2013;332:5748–65. doi:10.1016/j.jsv.2013.06.011.

[27] Xin G. Integrated design of vibration isolation and attitude control for high resolution remote sensing satellite. Tsinghua University; 2012. p. 54–6.

[28] Ekaterinaris JA. Numerical investigation of dynamic stall of an oscillating wing. AIAA J 1995;33:1803–8. doi:10.2514/3.12730.